University of Massachusetts Amherst

From the SelectedWorks of Gopal Narayanan

2008

The Five College Radio Astronomy Observatory CO Mapping Survey of the Taurus Molecular Cloud

Gopal Narayanan, *University of Massachusetts - Amherst*
Mark H. Heyer
Christopher Brunt
Paul F. Goldsmith
Ronald Snell, et al.

Available at: https://works.bepress.com/gopal_narayanan/12/

arXiv:0802.2556v1 [astro-ph] 18 Feb 2008

The Five College Radio Astronomy Observatory CO Mapping Survey of the Taurus Molecular Cloud

Gopal Narayanan[1], Mark H. Heyer[1], Christopher Brunt[1,2], Paul F. Goldsmith[3], Ronald Snell[1], Di Li[3]

gopal@astro.umass.edu

ABSTRACT

The FCRAO Survey of the Taurus Molecular Cloud observed the ^{12}CO and ^{13}CO J=1-0 emission from 98 deg^2 of this important, nearby star forming region. This set of data with 45″ resolution comprises the highest spatial dynamic range image of an individual molecular cloud constructed to date, and provides valuable insights to the molecular gas distribution, kinematics, and the star formation process. In this contribution, we describe the observations, calibration, data processing, and characteristics of the noise and line emission of the survey. The angular distribution of ^{12}CO and ^{13}CO emission over 1 km s^{-1} velocity intervals and the full velocity extent of the cloud are presented. These reveal a complex, dynamic medium of cold, molecular gas.

Subject headings: ISM: clouds — ISM: general — ISM: molecules — ISM: kinematics and dynamics — surveys

1. Introduction

The Taurus Molecular Cloud has long been a valued target for studies of star formation and the interstellar medium. Its proximity (140 pc) and displacement from the Galactic Plane (b∼-19°) afford high spatial resolution views of a star forming region with little or no confusion from background stars and gas. However, the large angular extent of the Taurus cloud (>100 deg^2) on the sky has limited most previous investigations to small, targeted areas or full coverage with coarse angular resolution. Given the complexity of the ISM and

[1]Dept. of Astronomy, Univ. of Massachusetts, Amherst MA 01003

[2]University of Exeter

[3]Jet Propulsion Laboratory, California Institute of Technology

the star formation process, such limited views may miss fine, structural features within the cloud or fail to recognize large scale patterns in the gas. Yet such structure provides critical clues to the prevailing physical processes that govern the formation of stars.

The sheer volume of the data that have been obtained and the number of analyses that have been carried out preclude giving a complete listing of the references to Taurus, so we will have to be selective rather than comprehensive, recognizing that we may have omitted many valuable contributions. The most complete inventory of the molecular gas content within the Taurus cloud is provided by Ungerechts & Thaddeus (1987), who observed ^{12}CO J=1-0 emission from 750 deg^2 of the Taurus-Auriga-Perseus regions. They estimate the molecular mass resident within the Taurus-Auriga cloud to be 3.5×10^4 M$_\odot$. However, the 30′ angular resolution of this survey precludes an examination of the small scale structure of the cloud. Targeted studies with higher angular resolution of ^{13}CO and C^{18}O emission from individual sub-clouds of Taurus reveal some of the relationships between the molecular gas, magnetic fields, and star formation but offer little insight to the coupling of these structures to larger scales and features (Schloerb & Snell 1984; Heyer et al. 1987; Mizuno et al. 1995; Onishi et al. 1996). Other studies have utilized other molecular tracers and even higher angular resolution to probe gas having different characteristics in some limited small regions of Taurus. Some examples include Langer et al. (1995) employing CCS, Onishi et al. (1996) and Onishi et al. (1998) using C^{18}O, Onishi et al. (2002) using H^{13}CO$^+$, and Tatematsu et al. (2004) employing N$_2$H$^+$. Many individual cores have been observed in NH$_3$, a tracer in which they appear well-defined, as indicated by the compilation of Jijina, Myers, & Adams (1999). The Leiden/Dwingeloo 21 cm study (Burton & Hartmann 1994) traced the atomic hydrogen towards Taurus, but with an angular resolution of 35′. One investigation (Shuter et al. 1987) used the Arecibo radio telescope having an angular resolution of 4′, but included only ∼1300 positions to probe the self–absorption seen in the 21 cm HI line. This cold atomic hydrogen appears to be associated with molecular gas (Li & Goldsmith 2003; Goldsmith & Li 2005), but the limited sampling of Shuter et al. does not reveal much about its morphology. The far–infrared emission from Taurus has been studied by Abergel et al. (1995), who also compared it to moderate resolution maps of ^{13}CO J = 1→0 emission. The dust column density distribution has been examined from 2MASS extinction by Padoan et al. (2002) and does bear a quite close resemblance to the integrated intensity of ^{13}CO, and thus to the column density of gas.

With the deployment of heterodyne focal plane arrays at millimeter and submillimeter wavelengths mounted on large or moderate-sized telescopes, it is possible to construct high spatial dynamic range, spectroscopic images of molecular line emission from interstellar clouds (Heyer 2000). In this contribution, we present the data from the spectroscopic imaging campaign of ^{12}CO and ^{13}CO J=1-0 emission obtained with the FCRAO 14m telescope and

the 32 element SEQUOIA focal plane array. The combined dataset of ^{12}CO and ^{13}CO allows us to make a much more accurate inventory of gas column density and mass for the Taurus molecular cloud than hitherto attempted. At high gas column densities, because of its greater optical depth, ^{12}CO is insensitive to variations in underlying column density. However, because of its higher abundance, it is effective in tracing much of the lower column density regions in the molecular cloud. The ^{13}CO transition, with its lower optical depth, allows us to probe deeper into the envelopes and trace the underlying structure of the molecular gas. Using both ^{12}CO and ^{13}CO we can derive the structure and column density of the molecular gas in different regimes of column density. The data from this survey constitute the most detailed view constructed to date of a molecular cloud and provides critical information for detailed studies of gas dynamics within the molecular interstellar medium. In this paper, we summarize the instrumentation, and data collection and analysis methods, and present global characteristics of noise and line emission from this survey. Detailed scientific motivation and results can be found in Goldsmith et al. (2008).

2. Observations

2.1. Instrumentation

All observations presented in this paper were taken with the 14 meter diameter millimeter-wavelength telescope and the 32 pixel focal plane array SEQUOIA (Erickson et al. 1999) of the Five College Radio Astronomy Observatory. The FWHM beam sizes of the telescope at the observed frequencies are 45″ (115.271202 GHz) and 47″ (110.201353 GHz). The main beam efficiencies at these frequencies are 0.45 and 0.50 respectively as determined from measurements of Jupiter. Previous measurements of the extended error beam of the telescope and radome structure by measuring the disks of the sun and moon indicate that there can be $\sim 25\%$ net contribution from extended emission outside the main beam from a region $\sim 0.5^\circ$ in diameter. The shape of this error beam is approximately circular, but the amount of contribution of emission at any given point from this error beam pattern depends on details of the distribution of the emission from the source. All data presented here are in T_A^* (K), uncorrected for telescope beam efficiencies. The backends were comprised of a system of 64 autocorrelation spectrometers each configured with 25 MHz bandwidth and 1024 spectral channels. No smoothing was applied to the autocorrelation function so the spectral resolution was 29.5 kHz per channel corresponding to 0.076 km s^{-1} (^{12}CO) and 0.080 km s^{-1}(^{13}CO) at the observed frequencies. The total coverage in velocity is 65 km s^{-1} (^{12}CO) and 68 km s^{-1} (^{13}CO) respectively. The spectrometers were centered at a v_{LSR} of 6 km s^{-1}.

2.2. Data Collection

The Taurus Molecular Cloud was observed over two observing seasons starting in November 2003 and ending in May 2005. The ^{12}CO and ^{13}CO lines were observed simultaneously enabling excellent positional registration and calibration. System temperatures ranged from 350-500 K for the ^{12}CO line and 150-300 K for the ^{13}CO line. The fiducial center position of the map was $\alpha(2000) = 04^h32^m44^s.6$, $\delta(2000) = 24°25'13''.08$. The $\sim$ 98 deg^2 selected region of the cloud was divided into 356 submaps, each $30' \times 30'$ in size. Each submap was observed using the On-The-Fly (OTF) mapping technique in which the telescope is continuously scanned back and forth along the Right Ascension axis while rapidly reading the spectrometers. The telescope was scanned at a rate such that 2 samples of data were collected while traversing the FWHM beam width at 115 GHz ($45''$). An additional ramping offset of $1'$ at the beginning and end of each scan was used to ensure stable motion of the antenna. OTF scans were spaced by $34''$ in declination. Since the SEQUOIA dewar is fixed with respect to the Azimuth-Elevation coordinate system, the scanning rate and declination offset between scan rows assured that the target field was densely sampled by the array. A given position on the sky was observed by most of the pixels in the array. Such redundant measurements increase the effective integration time at that position and also dilute the effects that arise from the small variations of noise and gain between the pixels of the array.

With a focal plane array and ramping offsets, there are data points that lie outside of the target $30'\times30'$ area. Upon convolution into a regularly spaced grid (see §2.3), these peripheral points contribute to the integration times of points located within but near the edge of the target area. To increase our mapping efficiency the submaps were spaced by $33'$, which enabled the peripheral spectra from contiguous submaps to be coadded with sufficient integration time to achieve the desired sensitivity. The target T_A^* sensitivities, σ, for each convolved (see §2.3) ^{12}CO and ^{13}CO spectrum were 0.65 K and 0.25 K respectively as gauged by the root-mean square of antenna temperature values within signal-free backend channels. The sensitivity of a submap was evaluated by the median rms value of σ, from the set of constituent spectra. Submaps with rms values in excess of 0.75 K were re-observed until the median value of σ of the co-added set of data was less than this maximum allowed value.

Position-switched spectral data requires a clean OFF position, which is free of line emission over the entire footprint of the SEQUOIA array. We used 5 different OFF positions spread around the Taurus molecular cloud. The right ascension and declinations of the OFF positions used in J2000 co-ordinates are ($04^h20^m00^s$, $23°00'00''$), ($04^h42^m00^s.9$, $23°25'41''$), ($04^h54^m22^s.7$, $24°43'28''$), ($04^h01^m15^s$, $27°32'00''$), and ($04^h20^m05^s.01$, $32°24'59''.2$). For any given submap observed, we typically chose the closest OFF position. The first two positions were known to be free of CO emission from previous studies. The other positions were

derived from constructing small maps in ^{12}CO and ^{13}CO at each position (a guess at an initial OFF was derived from the IRAS 100μm map). These maps were typically $10' \times 10'$ in size, and it was verified that ^{12}CO was not detectable to ~ 0.25 K level in the map.

In addition to the OTF maps, for each day of observing, pointing and focus measurements were made using a SiO maser source, IKTau ($03^h53^m28^s.81$, $11°24'22''.60$) every few hours. The pointing accuracy of the FCRAO 14 m telescope is typically better than $5''$. After each pointing observation, a single 80 second long position-switched observation in ^{12}CO and ^{13}CO was performed at the fiducial center position to keep track of the relative calibration accuracy of the whole survey (see §3.1).

For the observing campaign, a dynamic website with a relational database backend was created. From this website, the observing team could monitor the status of observations made to date, plan new observations, generate observing scripts, immediately reduce the OTF map after it was completed using a simple data reduction pipeline, view the integrated intensities of the spectra at the fiducial center position, and produce summary statistics of the map. The website also listed the sensitivities obtained in each submap, and produced prioritized list of submaps left to observe.

2.3. Data Processing

On-the-Fly mapping generates a set of data that is densely but irregularly sampled on the sky. To construct regularly sampled spectroscopic data cubes and to coadd spatially redundant measurements, the data were convolved into an output grid using a kernel that accounts for the edge taper of the 14m antenna to minimize noise aliasing, and retains the full angular resolution of the telescope. In addition to this spatial weighting, a spectrum was further weighted by the factor σ^{-2}, where σ is the measured rms noise. The spatial pixel separation in the regridded maps is $20''$.

Following this initial processing of submaps into data cubes, a systematic trend was present in the spectral baselines owing to gain drifts in the receiver. Each OTF scan begins with the measurement of OFF position, followed by two raster scanned rows of ON position observations, finally ending in an OFF position observation. The final spectra were computed using both OFF position observations weighting them equally. Spectra taken close in time to either of the OFF positions typically show a concave curvature in the baseline. While spectra taken approximately midway between the two OFFs typically show a convex curvature in baseline. These curvatures were small with respect to the noise of any single spectrum but were evident when averaging spectra with comparable time displacements from the off

measurement or when integrating individual spectra over velocity intervals comparable to the half period of the baseline curvature.

To rectify these baseline curvatures, we subtracted a baseline polynomial that depended on the spectral and sky coordinates of spectra within a given submap. We found that a second order polynomial along the spectral axis was sufficient and variations along the spatial axes could be adequately described by a first order polynomial. Accordingly, for each submap, we fit the parameterized baseline polynomial,

$$T_{base}(x, y, v) = \sum_{i=0}^{2} (v - v_\circ)^i f_i(x - x_\circ) g_i(y - y_\circ) \tag{1}$$

where $x_\circ, y_\circ, v_\circ$ are the central coordinates of the submap, and $f_i = a_i + b_i(x - x_\circ)$ and $g_i = c_i + d_i(y - y_\circ)$ parameterize the variation of the baseline curvature over the spatial axes. In the fitting procedure, we exclude the window $-5 < V_{LSR} < 15$ km s^{-1} that contains the spectral line emission from the Taurus Molecular Cloud.

This procedure has the advantage that only 12 parameters are required to specify the baselines for an entire submap, rather than the three per spectrum that would be needed for a standard baseline subtraction. All of the parameters are recorded so that the unbaselined data could be recovered if necessary. The fitting of a smooth baseline function to an entire submap also avoids the inadvertent removal of a broad, low-level, localized emission line component that could be produced by outflows and other energetic processes.

The maximum amplitudes of the baseline curvature were typically greater in the ^{13}CO data, where the most severe cases were still limited to levels less than 25 mK ($\sigma/10$). To demonstrate the need and effect of this baselining procedure, we show in Figure 1a ^{13}CO spectra averaged over $10' \times 10'$ boxes from a submap representative of the worse cases of baseline curvature. We emphasize that the curvature is not readily evident in a single spectrum. The thick solid lines show the fitted parameterized baselines averaged over the same boxes. The spatial variation in curvature is most significant along the scanning (x) direction, as noted above, with a slow drift in the y direction as the ON-OFF elevation difference varies during the 2-hour submap observation. Figure 1b shows the same average spectra after removal of the fitted baselines, with thick lines at zero intensity for reference.

The 356 regridded submaps, each of which have a size of $\sim 30' \times 30'$, were further consolidated into a set of larger data cubes. There are 88 such consolidated cubes, forming a grid of 11×8 data cubes, dubbed hard–edge cubes (as they do not have overlapping regions between two contiguous cubes). Each 'hard-edge' cube is assembled from a set of input regridded $30' \times 30'$ cubes, after removing the spectral and spatially derived baselines described above from each cube, and subsequently averaging the data together, weighting

them by σ^{-2}, where σ is the rms in the derived baseline. In angular offsets, the full extent of the combined hard–edge cubes are (5.75°, −5.75°) in RA offsets and (−2.75°, 5.75°) in Dec offsets from the fiducial center of the map. Thus for the full 11.5° × 8.5° region spaced at 20″, there are 3,167,100 spectra in each isotopologue in the combined set of hard–edge cubes. Most of the hard–edge cubes have a spatial size of 1 square degree, except for the cubes that lie on the four edges of the region covered, which measure 1.25 square degrees. The hard–edge cubes at the four corners of the Taurus map have a size of 1.5625 square degrees (1.25° × 1.25°).

3. Results

3.1. Calibration Uncertainty in Data

In order to track the relative calibration of the survey that was taken over the course of two observing seasons, we made position-switched (PS) measurements on the central (0,0) position every few hours. Since SEQUOIA does not rotate with the sky, only the (0,0) position was uniformly repeated. These (0,0) spectra were baseline subtracted and integrated over the velocity intervals 2-10 km s^{-1} and 3-9 km s^{-1} for ^{12}CO and ^{13}CO respectively to produce an integrated line intensity. Both the line profile shape and integrated intensity offer a cross check on the pointing and focus state of the telescope system. The set of these measurements also provide a quantitative measure of the calibration uncertainty of the data. Figure 2 shows the full set of measurements taken over the course of the survey. The mean and standard deviation, weighted by the statistical error for each spectrum, of the integrated intensity for both isotopologues are 12.5 ± 0.93 K km s^{-1} and 4.6 ± 0.43 K km s^{-1}. After subtracting the statistical uncertainties in quadrature, the estimated calibration uncertainties for ^{12}CO and ^{13}CO are 0.87 and 0.43 K km s^{-1} respectively, corresponding to a relative calibration uncertainty of 7% for ^{12}CO and 9.3% for ^{13}CO. Submaps that followed or preceded position switched measurements that significantly deviated from these mean values were reobserved.

4. Noise Properties

Quantitative measures of cloud structure rely on the sensitivity of the data, its uniformity across the target field, and the underlying noise characteristics of the data. For individual submaps, On-the-Fly Mapping with a focal plane array produces near uniform sensitivity over most of the field. Toward the edges of the submap, the noise necessarily

increases as there is less integration time accumulated at these positions. However, our placement of submaps ensured that there are sufficient overlaps of contiguous fields so that these spectra accumulated additional integration time. Indeed, upon the construction of the 1 deg^2 cubes, the sensitivity of these "edge" spectra is comparable or better than the spectra from the central parts of any submap.

For a given spectrum, the statistical error of the antenna temperature at any channel, σ, is conventionally estimated from the standard deviation of antenna temperatures within intervals in which no signal is present. This measure includes noise contributions from the instrument and atmosphere. For the Taurus Survey, we have calculated σ for all the co-added convolved and resampled ^{12}CO and ^{13}CO spectra excluding values within the velocity range of the Taurus cloud (-5 $< V_{LSR} <$ +15 km s^{-1}). The cumulative distributions of $\sigma(^{12}CO)$ and $\sigma(^{13}CO)$ are shown in Figure 3. The steepness of these distributions provides an approximate measure of noise uniformity. The first, second, and third quartile values are 0.53 K, 0.58 K, and 0.63 K for ^{12}CO and 0.23 K, 0.26 K, and 0.28 K for ^{13}CO.

The antenna temperature distribution of all voxels within the data cube offers another measure of the noise properties. In Figure 4, this distribution is shown for the composite ^{12}CO and ^{13}CO data cubes of the survey. For both data cubes, statistical noise contributes to the peak component centered on T_A^*=0.0 K. Signal from the Taurus cloud is responsible for the excess positive emission. In the ideal case in which all spectra have gaussian distributed fluctuations with constant rms value, σ, the dispersion of the voxel distribution about T_A^*=0 K would be equivalent to σ. More realistically, the noise is not uniform and not necessarily gaussian. For example, the use of a common reference position for many source spectra introduces correlated noise. With OTF mapping using a focal plane array, where a given position on the sky is sampled by many pixels in the array, this effect is present but not as severe as discrete mapping methods that share reference positions (Heyer et al. 1998; Jackson et al. 2006). As shown in Figure 3, the noise of this survey is not uniform. To assess departures from the gaussian character of the distribution of noise in the ^{12}CO and ^{13}CO data, we have generated equivalently sized data cubes filled with gaussian noise values that follow the same distribution of σ values shown in Figure 3. The respective distributions of these purely gaussian noise spectra, shown as the dotted lines in Figure 4, provide an excellent match to the zero-centered noise components. We conclude that the noise measured in the ^{12}CO and ^{13}CO data cubes can not be readily distinguished from pure gaussian noise. It is dominated by statistical fluctuations from the receiver and the sky rather than by systematic contributions.

5. Images

Two dimensional images are generated from the spectroscopic data cubes by reducing the information of each spectrum to a single scalar value. These reductions include maps of maximum value, the integration of spectra over a set of velocity intervals (zero moment), and higher moments such as the centroid velocity or line width. To convey a fraction of the information resident within these data cubes, we show some of these reductions in images of the Taurus Cloud.

Zero moment images derived from the ^{12}CO and ^{13}CO data cubes over the V_{LSR} range 0 to 12 km s^{-1} in 1 km s^{-1} intervals are presented in Figure 5. The two images show quite distinct distributions between the two isotopologues. The ^{12}CO J=1-0 integrated emission is mostly diffuse, even towards the three known primary sub clouds of Taurus (Heiles' Cloud 2, Barnard 18, L1495). In the most faint regions, there are weak "streaks" or striations of ^{12}CO emission that are typically aligned with the local magnetic field direction (Goldsmith et al. 2008; Heyer et al. 2008). The ^{13}CO J=1-0 emission is mostly distributed within high contrast filaments. However, even within the diffuse regions, the weak ^{13}CO emission exhibits a striated pattern. These differences between the ^{12}CO and ^{13}CO distributions can be readily attributed to the higher opacity of the ^{12}CO emission that likely limits its probed volume to the low column density envelope of the cloud. Images of peak ^{12}CO and ^{13}CO intensity are shown in Figure 6. For the optically thick ^{12}CO line, the peak intensity is a valuable measure of the excitation temperature.

In Figures 7-19, we show the distribution of ^{12}CO and ^{13}CO J=1-0 emission averaged over 1 km s^{-1} velocity intervals centered at V_{LSR} 0.5, 1.5, 2.5 ... 12.5 km s^{-1}. As noted by many previous studies (Brunt & Mac Low 2004; Lazarian & Pogosyan 2000), more of the emission is found at the higher spatial frequencies when integrating over small velocity intervals. The structure that is measured arises from variations in the velocity field rather than those of density or column density (Brunt & Mac Low 2004). These narrow velocity integrated images reveal stunning textural patterns and individual features that occur over a broad range of scales. There are regions of faint, low surface brightness emission, most notably evident in the ^{12}CO data. Often, this emission component exhibits low amplitude striations that are similar to the wind swept structures observed within terrestrial cirrus clouds. Owing to lower optical depth, the ^{13}CO emission shows more high contrast emission originating from higher column density regions located deeper within the cloud. The feature located within the southwest corner with $V_{LSR} \sim 10$ km s^{-1} in Figure 16 may not be associated with the Taurus cloud.

6. Box Averaged Spectra

To convey the coarse velocity field of the cloud and to further emphasize the quality of the data, we have constructed average ^{12}CO and ^{13}CO J=1-0 spectra from each 1, 1.25, or 1.56 deg^2 cube. These are shown in Figure 20 overlayed upon images of integrated intensity. Each spectrum is an average of 32,400, 40,500, or 50,625 individual spectra with typical rms values of 0.014 K for ^{12}CO and 0.006 K for ^{13}CO (T_A^*). These rms values are greater than one would expect averaging this number of spectra each with the respective median values shown in Figure 3. This discrepancy arises from spatially correlated noise imposed on spectra sharing a common reference measurement in the OTF data collection scheme. The average spectra demonstrate excellent baseline fidelity with no evidence for any systematic noise contribution.

The average spectra do reveal several significant properties of the Taurus velocity field. The previously established large scale velocity gradient across the Taurus Molecular Cloud is apparent in the systemic shift of the spectra from blueshifted velocities on the eastern side to redshifted velocities on the western portion of the cloud. In addition, many of the average spectra exhibit asymmetries and multiple velocity components that attest to the complex structure along the line of sight.

7. Emission Statistics

The ^{12}CO and ^{13}CO data cubes of Taurus provide panoramic views of the structure of a 10^4 $M_\odot$ molecular cloud. The resident information is sufficiently vast to require statistical descriptions of the data that may offer insight to the prevailing conditions or state of the cloud. The cumulative probability density function is defined to be

$$P(f_\circ) = \frac{\int\int dxdyF(x,y,f_\circ)}{\int\int dxdyF(x,y,f_{max})} \qquad (2),$$

where

$$F(x,y,f_\circ) = \begin{cases} 0 & \text{for } f(x,y) > f_\circ \\ 1 & \text{for } f(x,y) \leq f_\circ, \end{cases}$$

with $f(x,y)$ the 2 dimensional distribution of some measured parameter, $f_\circ$ a moving threshold of that parameter, and f_{max} the maximum value of the measured parameter in the whole map. The weighted cumulative PDF biases each bin of $f(x,y)$ by the total signal, $\int T(x,y,v)dv$, of all contributing pixels,

$$P_w(f_\circ) = \frac{\int\int dxdyF(x,y,f_\circ)\int T(x,y,v)dv}{\int\int dxdy\int T(x,y,v)dv} \qquad (3)$$

Figures 21 and 22 show the cumulative PDF and weighted cumulative PDF for integrated intensity (denoted as W(^{12}CO) and W(^{13}CO) respectively), and peak temperature distributions (denoted as T_{max}(^{12}CO) and T_{max}(^{13}CO) respectively). The weighting function used is the corresponding integrated intensity. The unweighted cumulative PDF shows the cumulative fraction of projected area as a function of integrated intensity (Figure 21) and peak temperature (Figure 22). The weighted cumulative PDF shows the cumulative fraction of integrated intensity as a function of integrated intensity (Figure 21) and peak temperature (Figure 22). The median values for the weighted PDFs of integrated intensity are 6.9 and 1.9 K km s^{-1} for ^{12}CO and ^{13}CO respectively. Similarly, for peak temperature, the weighted median values are 4.1 K and 1.9 K. These figures demonstrate that much of the ^{12}CO and ^{13}CO signal originates from lines of sight within the low surface brightness regime of the Taurus cloud. For example, the weighted cumulative PDFs demonstrate that half of the ^{12}CO flux of a cloud is emitted within the low surface brightness portion of the Taurus molecular cloud having ^{12}CO integrated intensity less than 6.9 K km s^{-1} and peak temperature $\leq$ 4.1 K. In terms of projected area, only $\sim$ 20% of the cloud's area has integrated intensity $\geq$ 6.9 K km s^{-1} or peak temperature $\geq$ 4.1 K in ^{12}CO.

8. Conclusions

The FCRAO Survey of the Taurus Molecular Cloud is a powerful set of data to investigate interstellar gas dynamics and the star formation process with high spatial resolution and spatial dynamic range. It offers a valuable complement to observations at other wavelengths that probe the dust component and the population of young stellar objects. In this paper, we summarized the instrumentation, data collection and processing procedures used in the survey. We also characterized the noise and signal distributions of the survey. The overall structure of the cloud, its column density distribution and mass, and relationship with the magnetic field are discussed in Goldsmith et al. (2008).

This work was supported by NSF grant AST 05-40852 to the Five College Radio Astronomy Observatory, NSF grant AST-0407019 to Cornell University, and by the Jet Propulsion Laboratory, California Institute of Technology. We thank Yvonne Tang and Marko Krco for for assistance with observations.

REFERENCES

Abergel, A., Boulanger, F., Fukui, Y., & Mizuno, A. 1995, A&A, 111, 483

Brunt, C.M. & Mac Low, M. 2004, ApJ, 604, 196

Burton, W.B. & Hartmann, D. 1994, in Unveiling Large–Scale Structures Behind the Milky Way, ASP Conf. Serives, Vol. 67, C. Balkowski & R.C. Kraan-Kortweg eds. (San Francisco: Astronomical Society of the Pacific), 31

Erickson, N.R.. Grosslein, R.M., Erickson, R.B., & Weinreb, S. 1999, IEEE Trans. Microwave Theory Tech., 47(12), 2212

Goldsmith, P.F. & Li, D. 2005, ApJ, 622, 938

Goldsmith, P. F., Heyer, M. H., Narayanan, G., Snell, R. L., Li, D., & Brunt, C., 2008, to be submitted to ApJ

Heyer, M.H., Vrba, F., Snell, R.L., Schloerb, F.P., Strom, S.E., Goldsmith, P.F., & Strom, K.M. 1987, ApJ, 321, 855

Heyer, M.H., Brunt, C., Snell, R.L., Howe, J.E., Schloerb, F.P., Carpenter, J.M. 1998, ApJS, 115, 241

Heyer, M. H. 2000, Imaging at Radio through Submillimeter Wavelengths, 217, 213

Heyer, M.H., Gong, H., Ostriker, E., & Brunt 2008, submitted to ApJ

Jackson, J. M., Rathborne, J. M., Shah, R. Y., Simon, R., Bania, T. M., Clemens, D. P., Chambers, E. T., Johnson, A. M., Dormody, M., Lavoie, R., Heyer, M. H. 2006, ApJS, 163, 145

Jijina, J., Myers, P.C., & Adams, F.C. 1999, ApJS, 125, 161

Langer, W.D., Velusamy, T., Kuiper, T.B.H., Levin, S., Olsen, E., & Migenes, V. 1995, ApJ, 453, 293

Lazarian, A., & Pogosyan, D. 2000, ApJ, 537, 720

Li, D. & Goldsmith, P.F. 2003, ApJ, 585, 823

Mizuno, A., Onishi, T., Yonekura, Y., Nagahama, T., Ogawa, H., & Fukui, Y. 1995, ApJ, 445, L161

Onishi, T., Mizuno, A., Kawamura, A., Ogawa, H., Fukui, Y. 1996, ApJ, 465, 815

Onishi, T., Mizuno, A., Kawamura, A., Ogawa, H., & Fukui, Y. 1998, ApJ, 502, 296

Onishi, T., Mizuno, A., Kawamura, A., Tachihara, K., & Fukui, Y. 2002, ApJ, 575, 950

Padoan, P., Cambrésy, L., & Langer, W.D. 1992, ApJ, 580, L57

Schloerb, F.P. & Snell, R.L. 1984, ApJ, 283, 129

Shuter, W.L.H., Dickman, R.L., & Klatt, C. 1987, ApJ, 322, L103

Tatematsu, K., Umemoto, T., Kandori, R., & Sekimoto, Y. 2004, ApJ, 606, 333

Ungerechts, H. & Thaddeus, P. 1987, ApJ, 322, 706

This preprint was prepared with the AAS LaTeX macros v5.2.

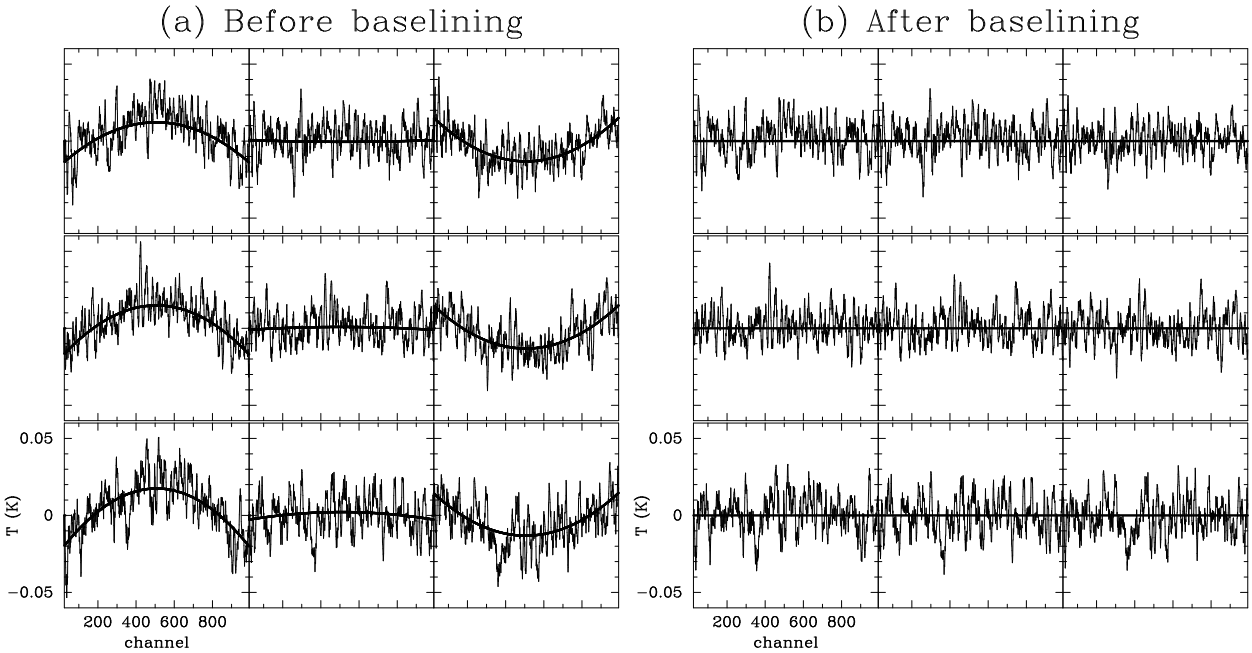

Fig. 1.— (a) ^{13}CO spectra in a $30' \times 30'$ region averaged over $10' \times 10'$ and fitted parameterized baselines (thick lines). The rightmost column of spectra corresponds to observations taken close in time to an OFF measurement, while the leftmost column corresponds to spectra taken farthest in time from an OFF observation. The middle column represents a time in between these extremes. See the text for details. (b) The same box–averaged spectra after baseline removal, with thick lines at zero intensity for reference.

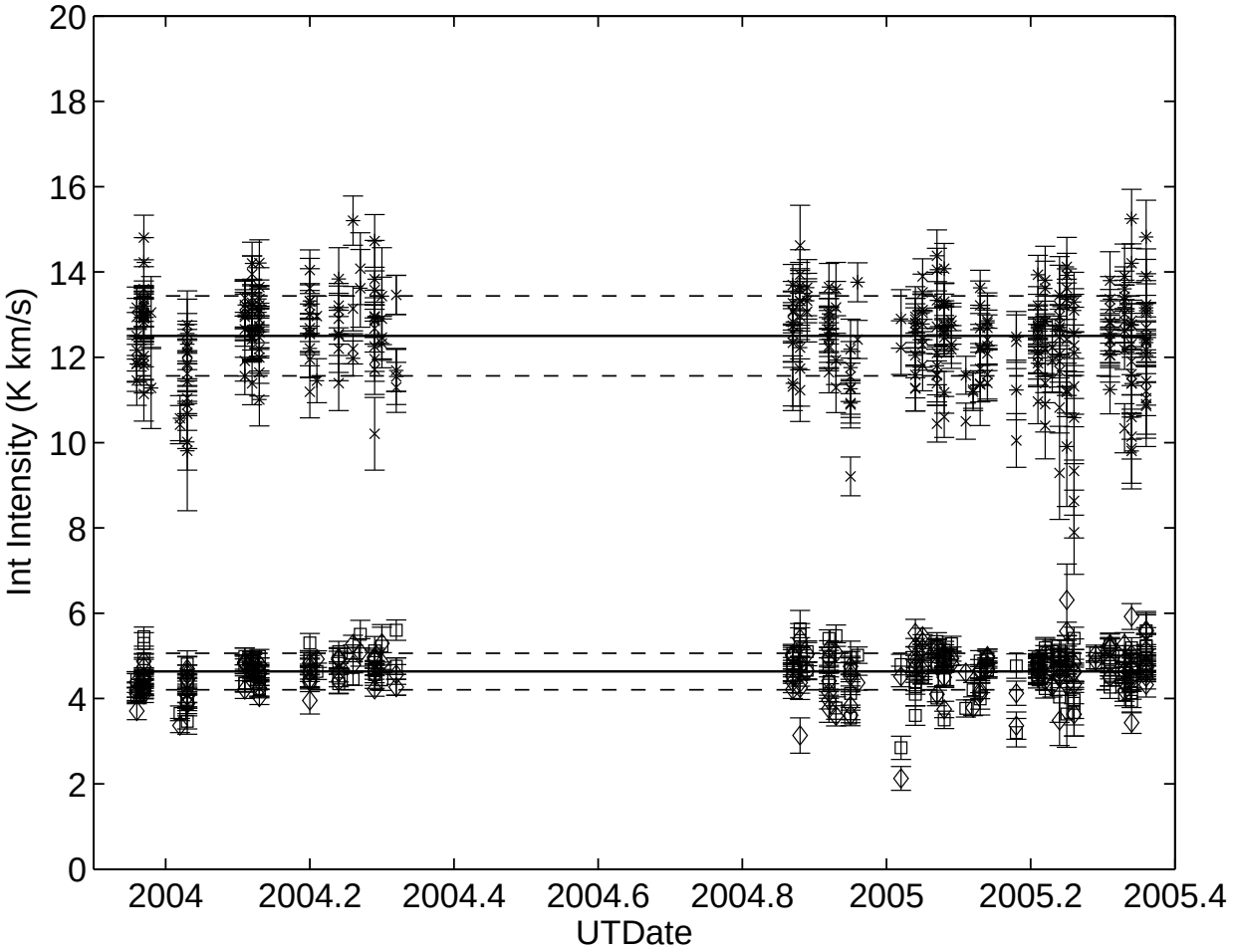

Fig. 2.— Integrated intensity in the position-switched spectra for the (0,0) position for both polarizations and both isotopologues over the entire observing period. The ^{12}CO data have integrated intensity $\simeq 12.5$ K km s^{-1}and the ^{13}CO data have integrated intensity $\simeq 4.6$ K km s^{-1}. The error bars denote 1σ statistical errors in these values. The ^{12}CO data are denoted by crosses and plus symbols and the ^{13}CO data by squares and diamonds, for the two polarizations. The horizontal solid lines show the mean integrated intensities derived for each data set and the dashed lines indicate $\pm$ standard deviation about these mean values. The gap in coverage in the middle of year 2004 is due to the normal summer shutdown period of the FCRAO 14 m telescope.

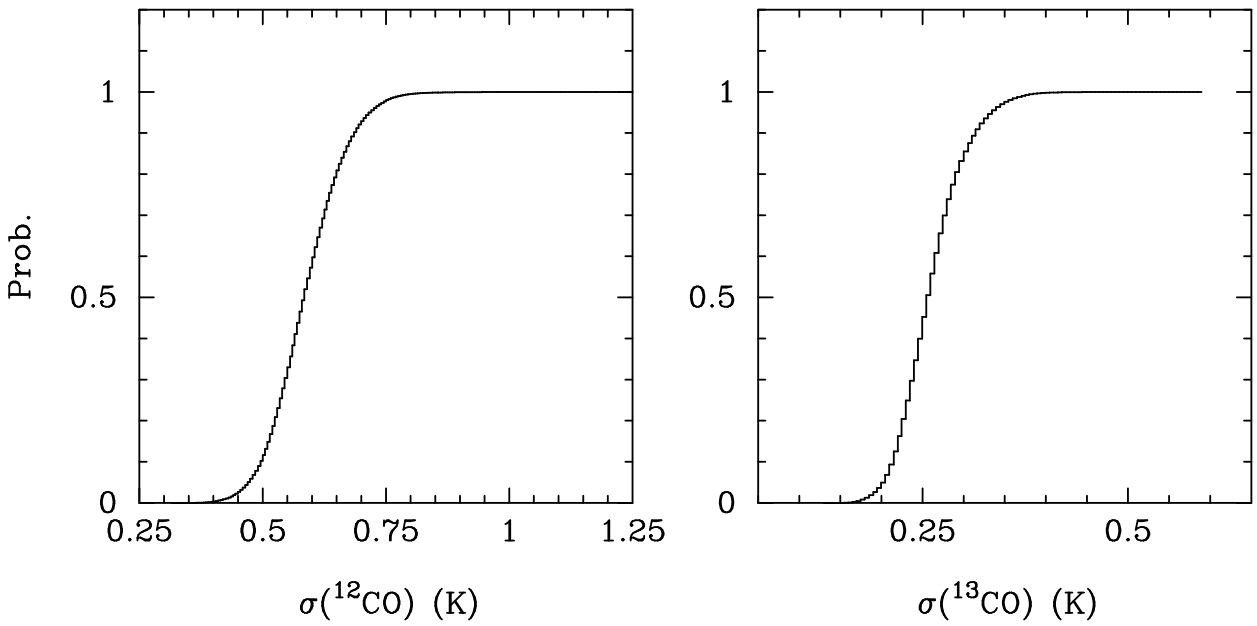

Fig. 3.— Cumulative distributions of rms values, $\sigma(^{12}\mathrm{CO})$ and $\sigma(^{13}\mathrm{CO})$ derived from signal–free channels within the Taurus ^{12}CO and ^{13}CO data cubes.

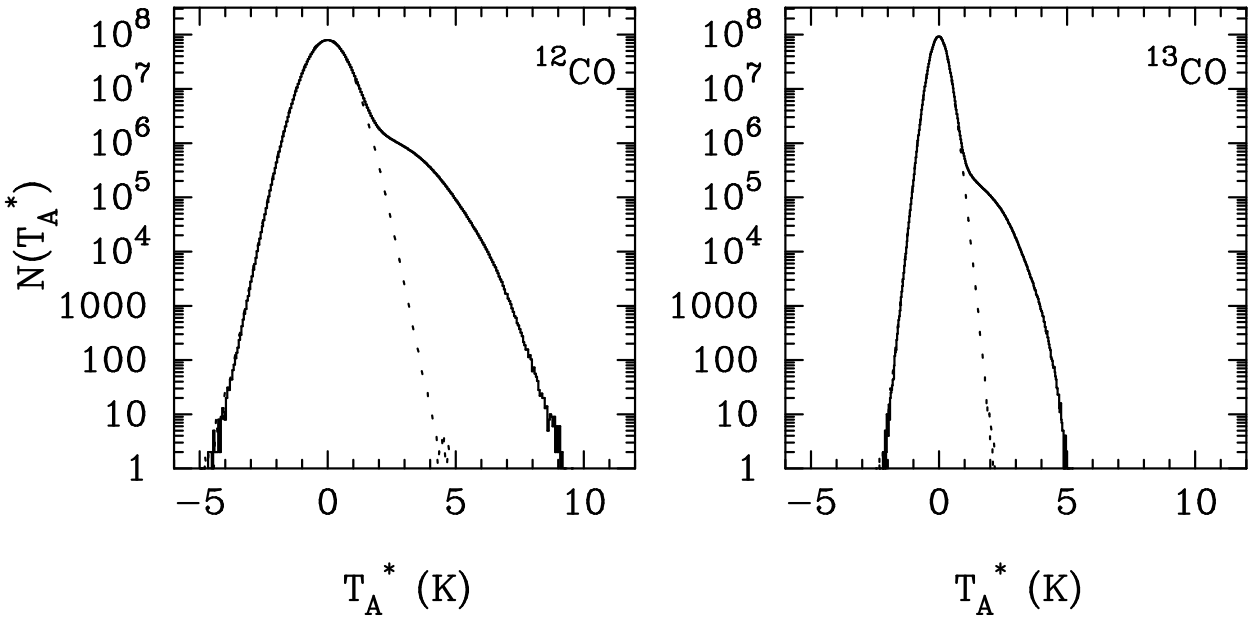

Fig. 4.— The distribution of voxel values within the composite ^{12}CO and ^{13}CO data cubes (solid lines). The dotted lines show the distribution of values obtained from data cubes of equal size containing only gaussian noise with values of σ that follow the same distribution shown in Figure 3. These provide an excellent fit to the data and demonstrate the near gaussian character of the noise of individual spectra.

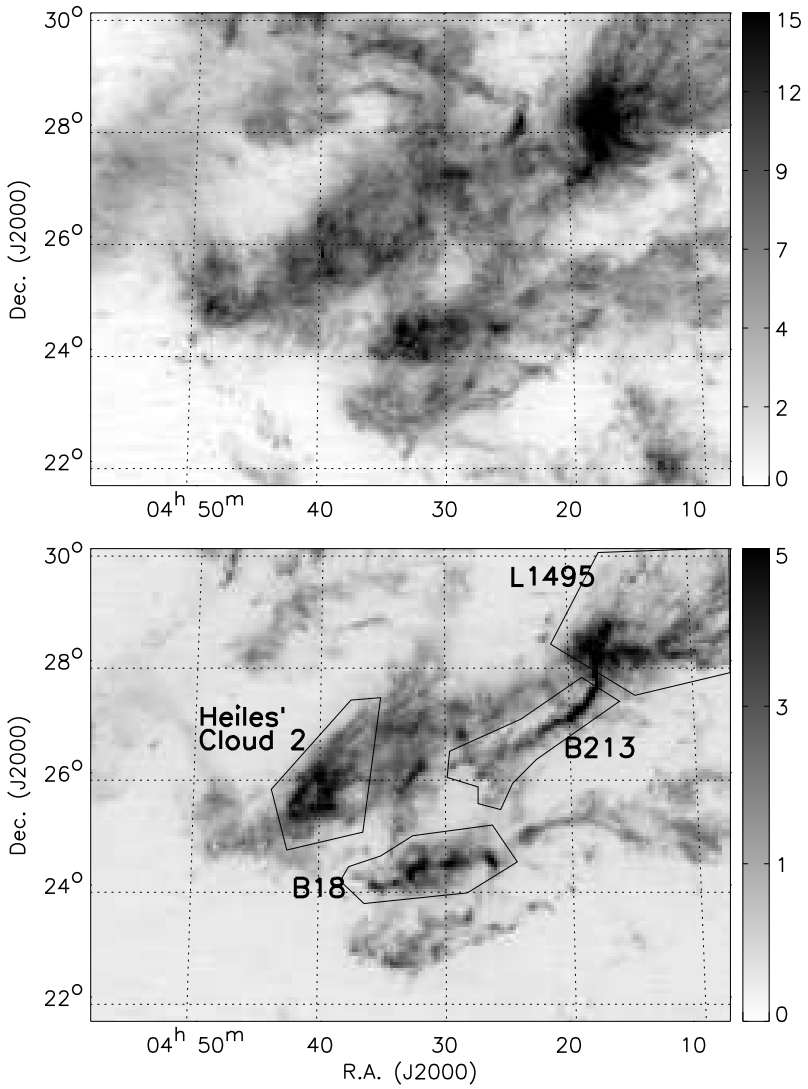

Fig. 5.— Integrated Intensity Images for ^{12}CO (top) and ^{13}CO (bottom). The images are obtained over -5 to 20 km s^{-1} and 3 to 9 km s^{-1} for ^{12}CO and ^{13}CO respectively. The colorbar on the right shows the integrated intensity scale in K.km s^{-1}. In the ^{13}CO figure, we also overlay outlines of a few well-known regions in Taurus as designated by Onishi et al. (1996).

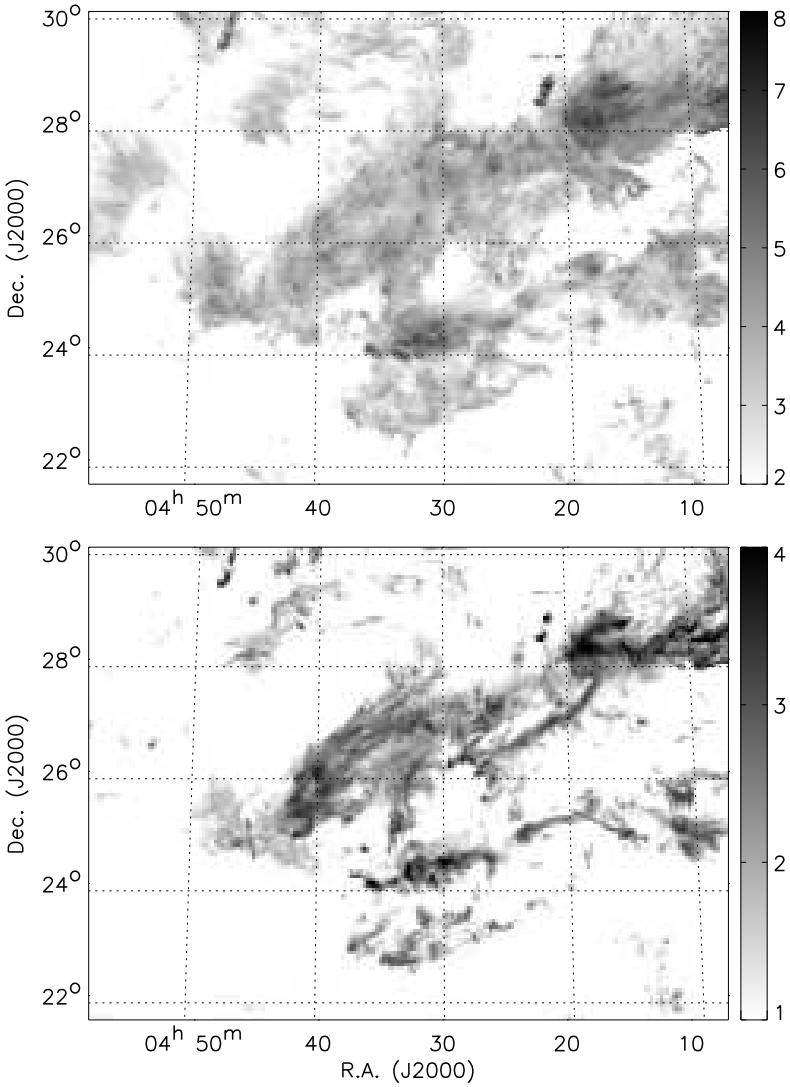

Fig. 6.— Images of peak intensity, T_{max}, for ^{12}CO (top) and ^{13}CO (bottom). The peak temperature in the velocity range of 0 to 12 km s^{-1} is used in both cases. The colorbar on the right shows the T_{max} scale in antenna temperature units (K).

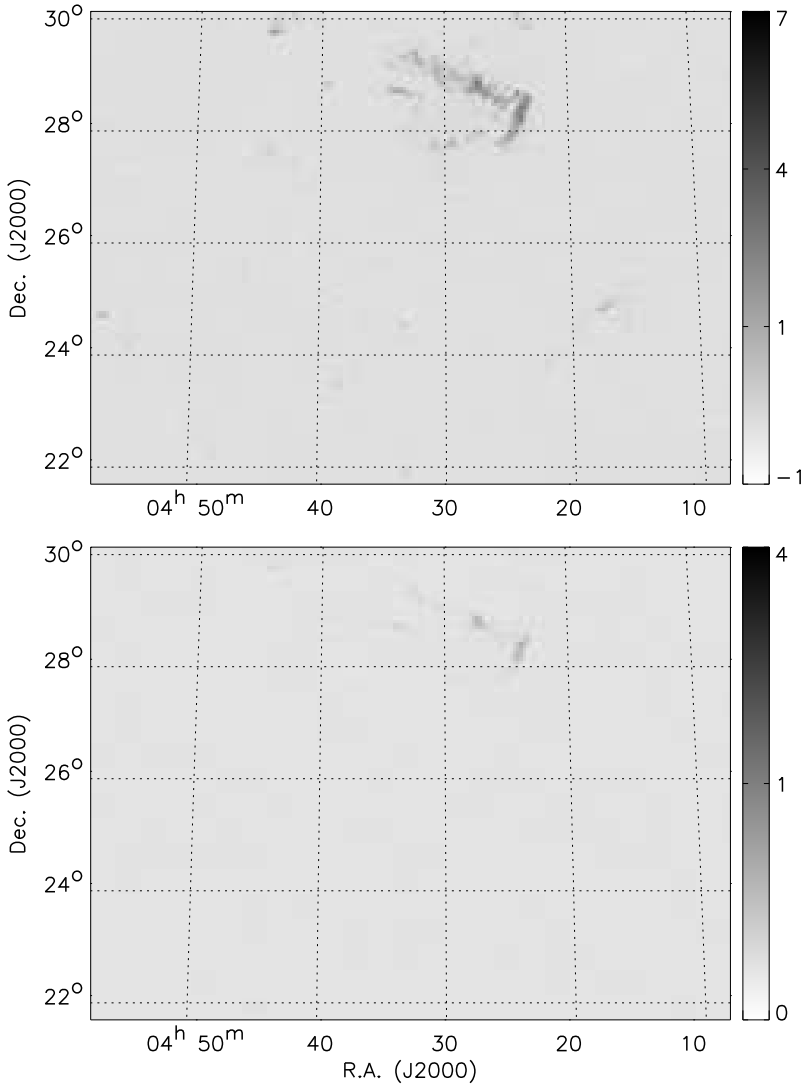

Fig. 7.— Images of ^{12}CO (top) and ^{13}CO (bottom) emission integrated between V_{LSR} 0 to 1 km s^{-1}.

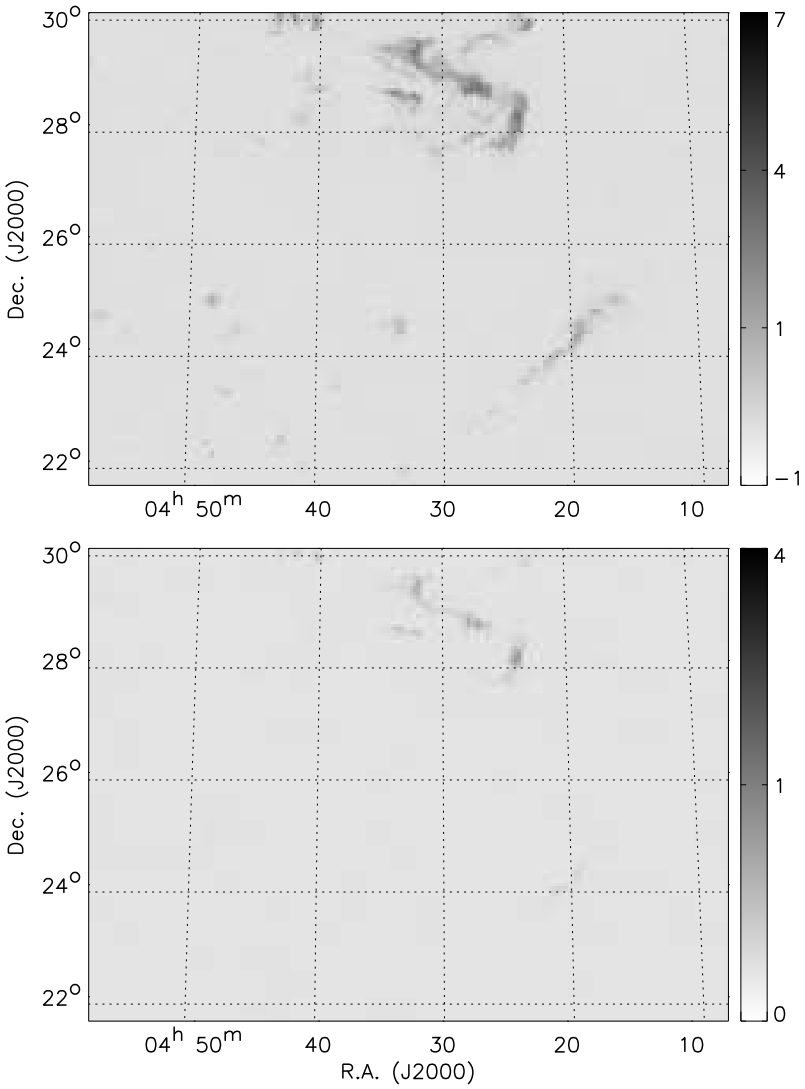

Fig. 8.— Same as Figure 7 for V_{LSR} 1 to 2 km s^{-1}.

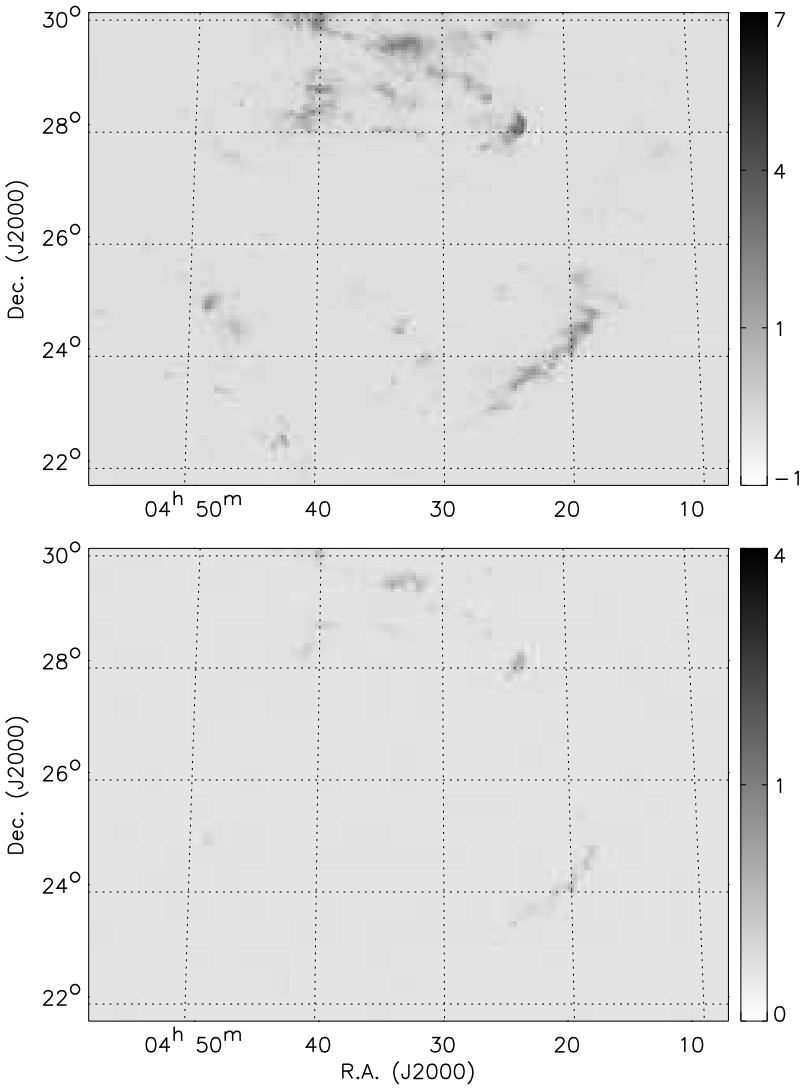

Fig. 9.— Same as Figure 7 for V_{LSR} 2 to 3 km s^{-1}.

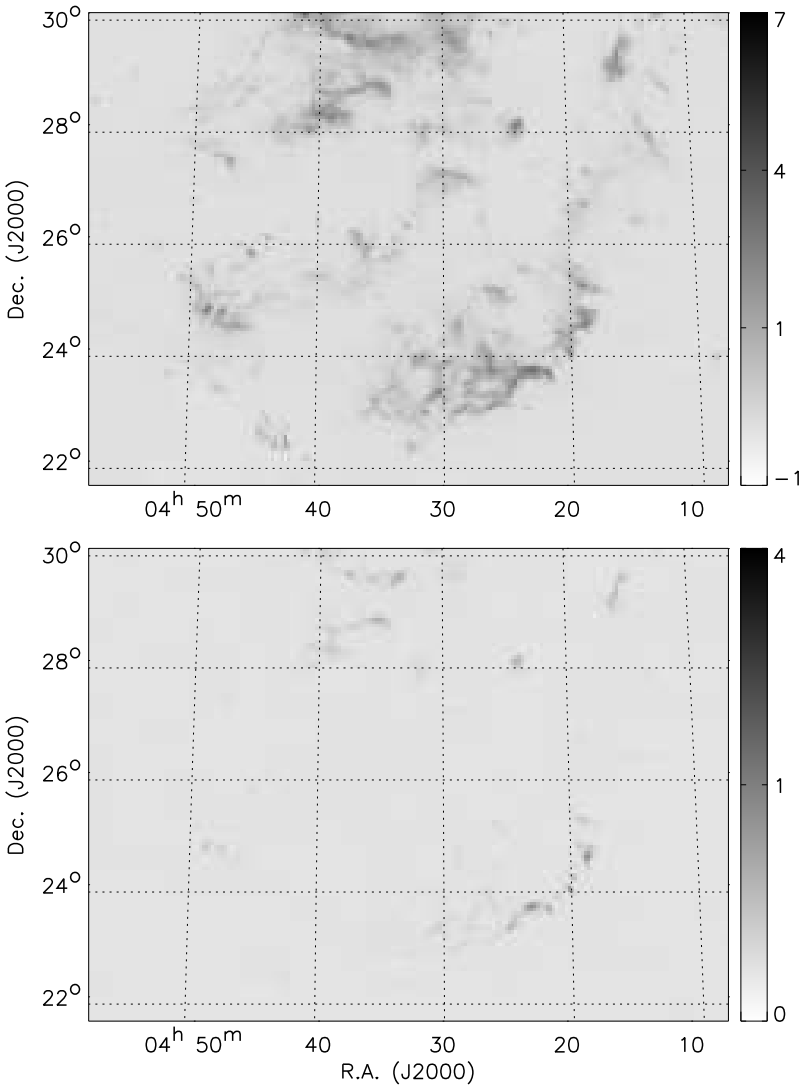

Fig. 10.— Same as Figure 7 for V_{LSR} 3 to 4 km s^{-1}.

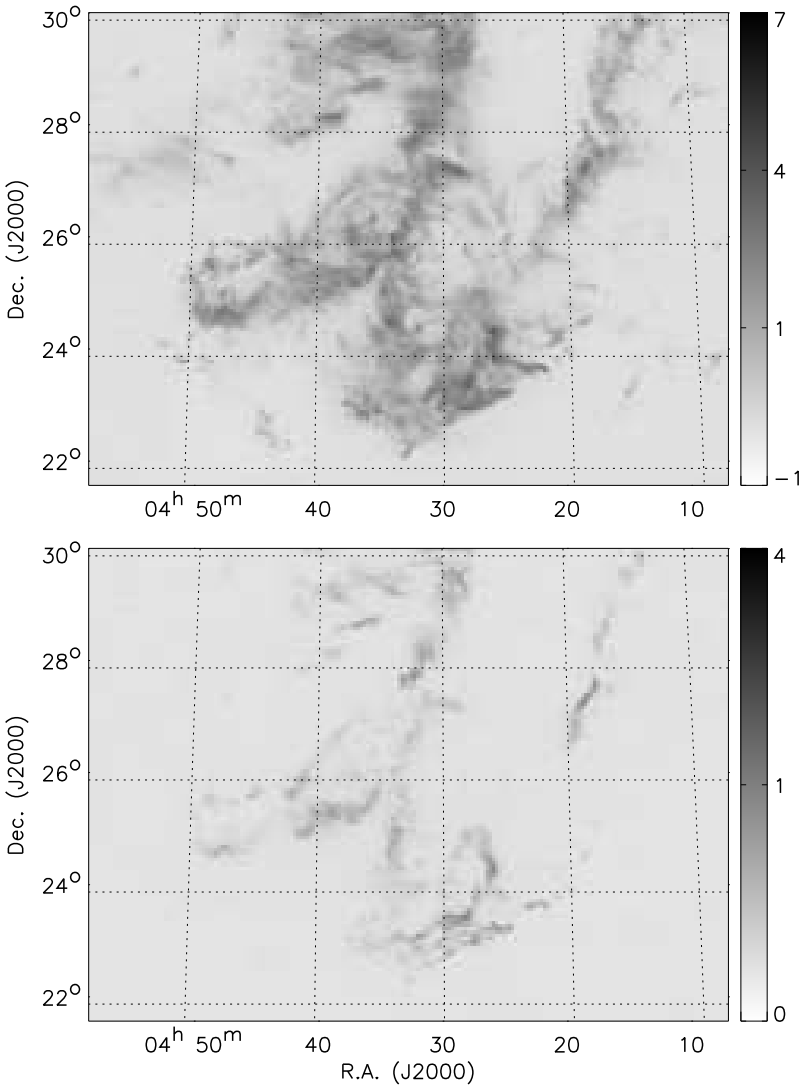

Fig. 11.— Same as Figure 7 for V_{LSR} 4 to 5 km s^{-1}.

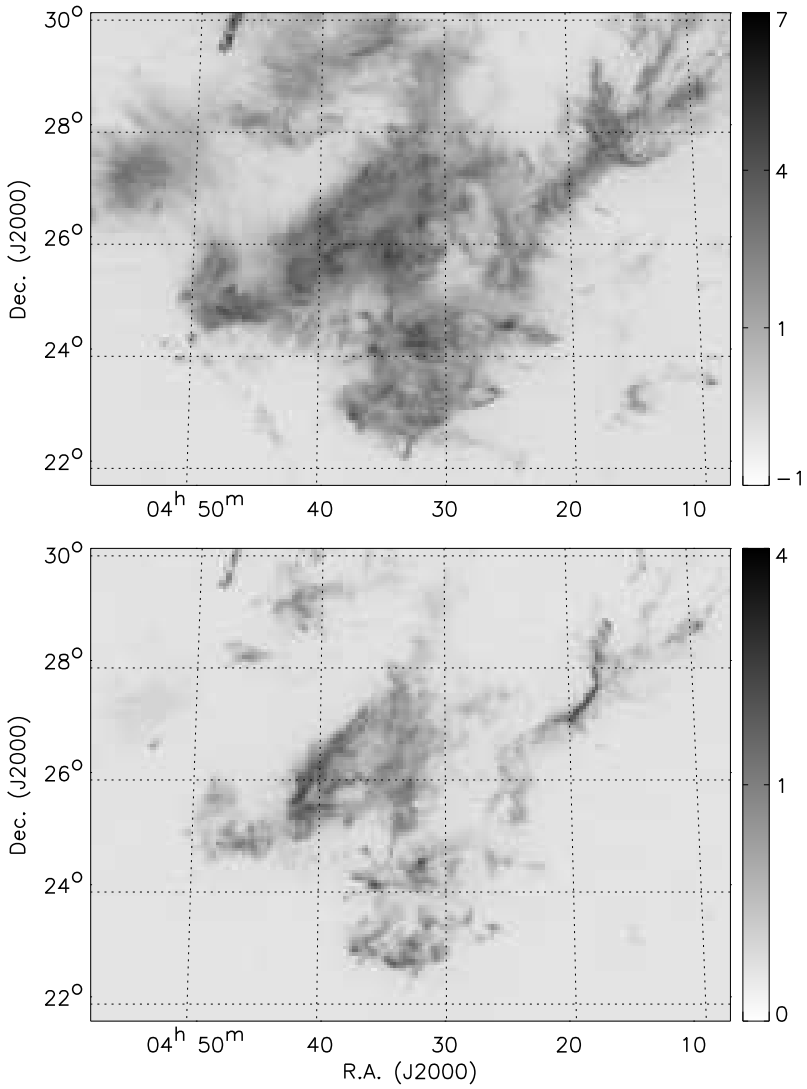

Fig. 12.— Same as Figure 7 for V_{LSR} 5 to 6 km s^{-1}.

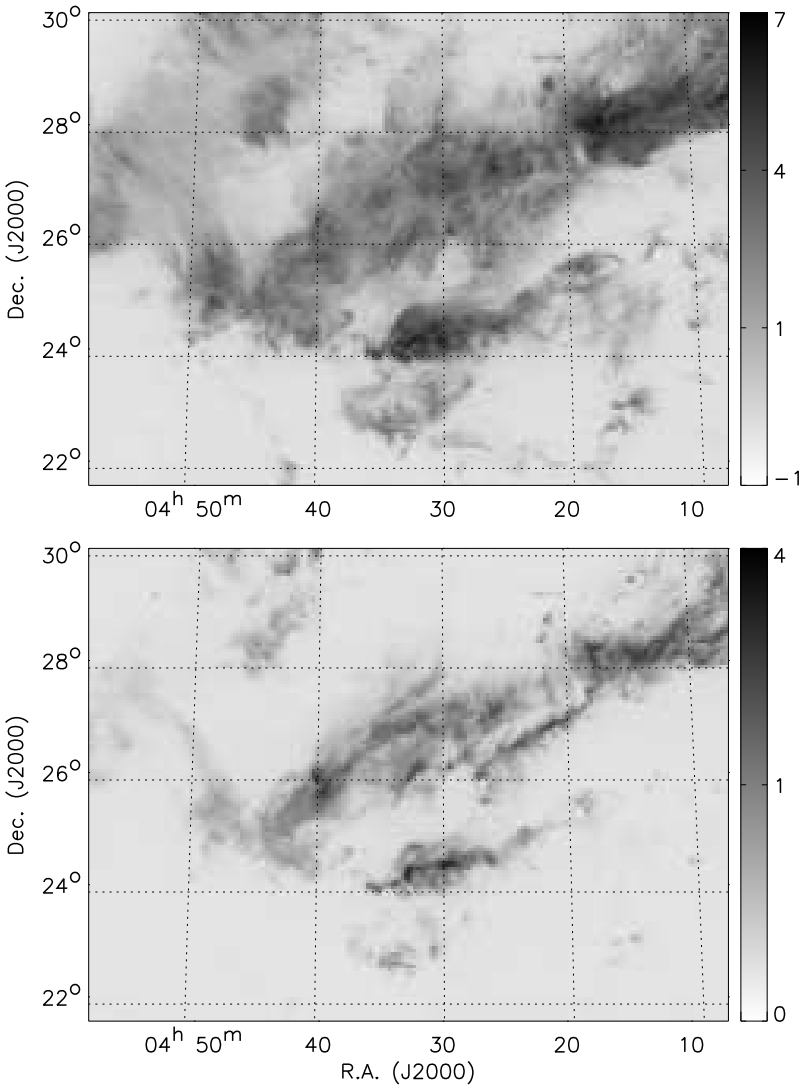

Fig. 13.— Same as Figure 7 for V_{LSR} 6 to 7 km s^{-1}.

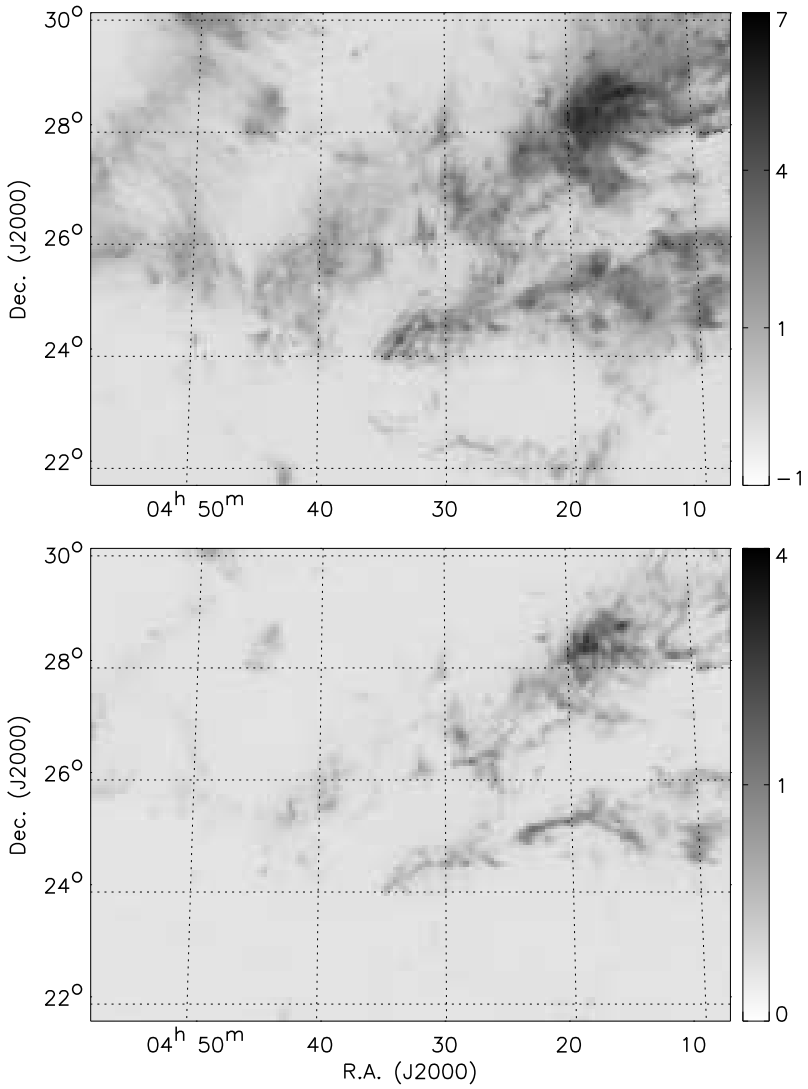

Fig. 14.— Same as Figure 7 for V_{LSR} 7 to 8 km s^{-1}.

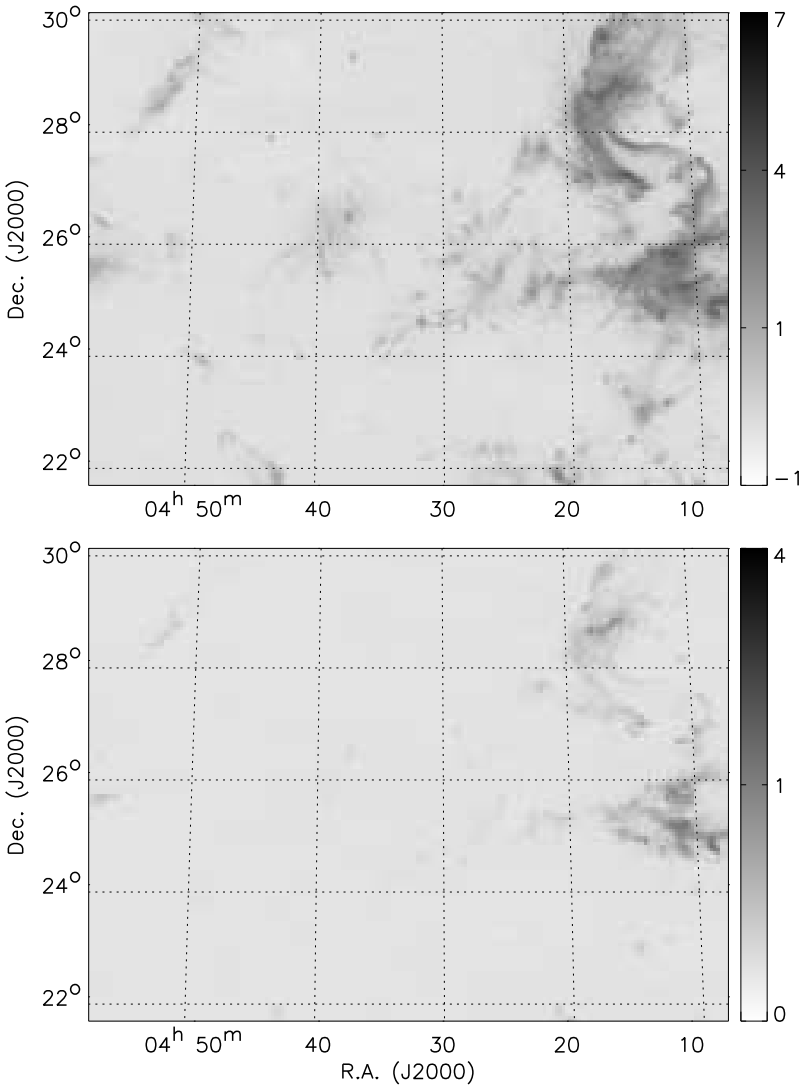

Fig. 15.— Same as Figure 7 for V_{LSR} 8 to 9 km s^{-1}.

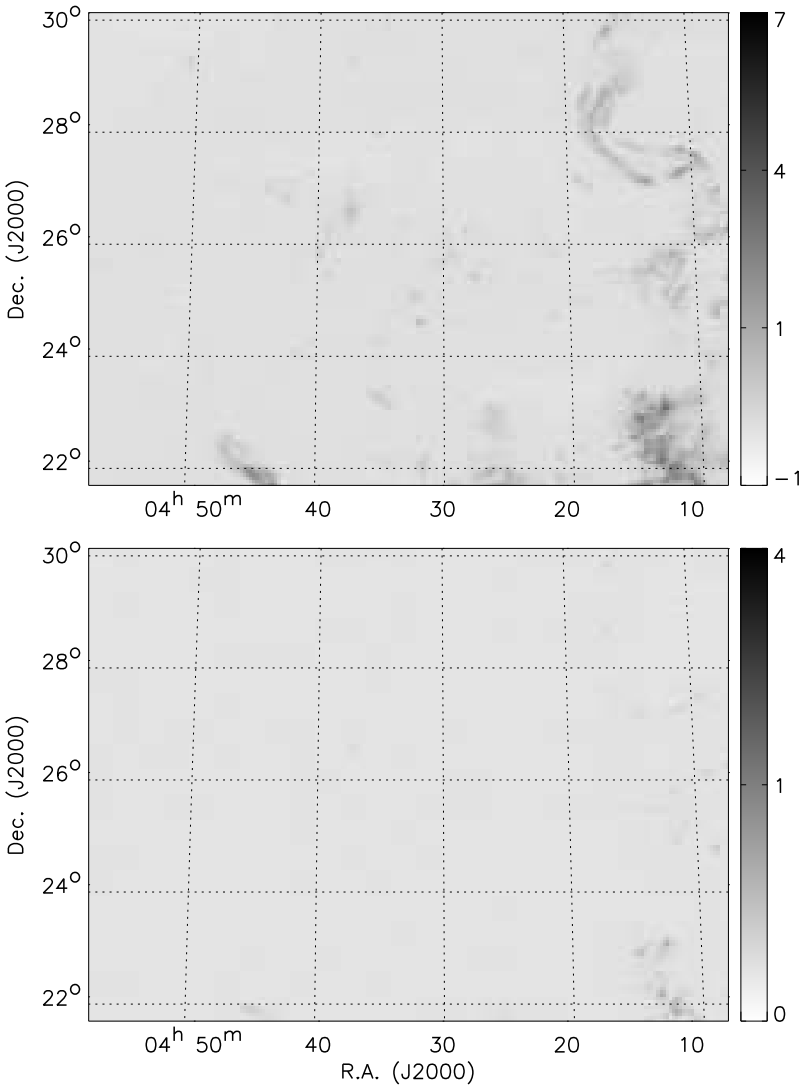

Fig. 16.— Same as Figure 7 for V_{LSR} 9 to 10 km s^{-1}.

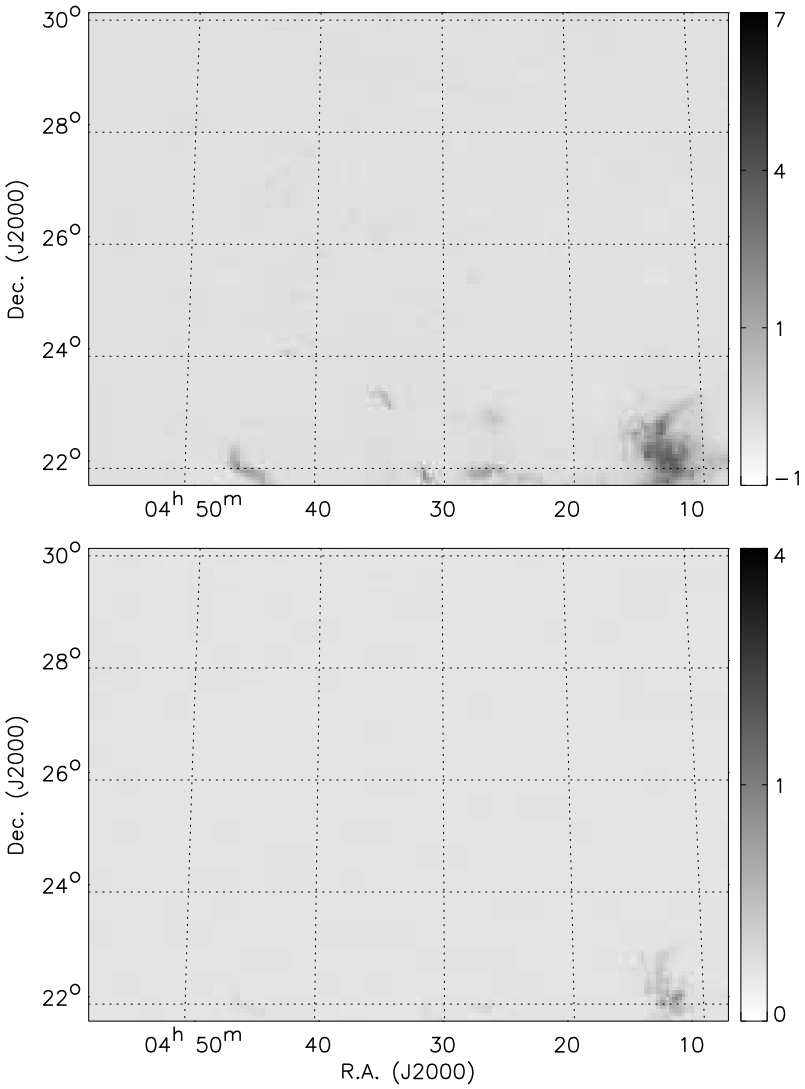

Fig. 17.— Same as Figure 7 for V_{LSR} 10 to 11 km s^{-1}.

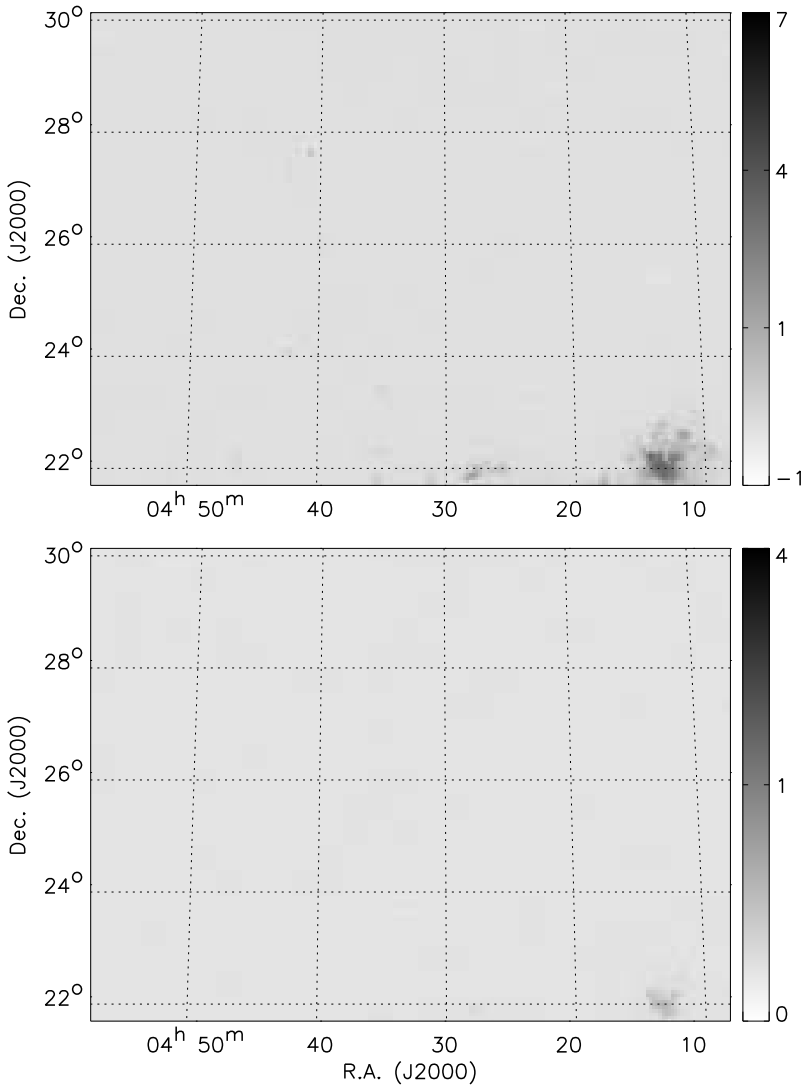

Fig. 18.— Same as Figure 7 for V_{LSR} 11 to 12 km s^{-1}.

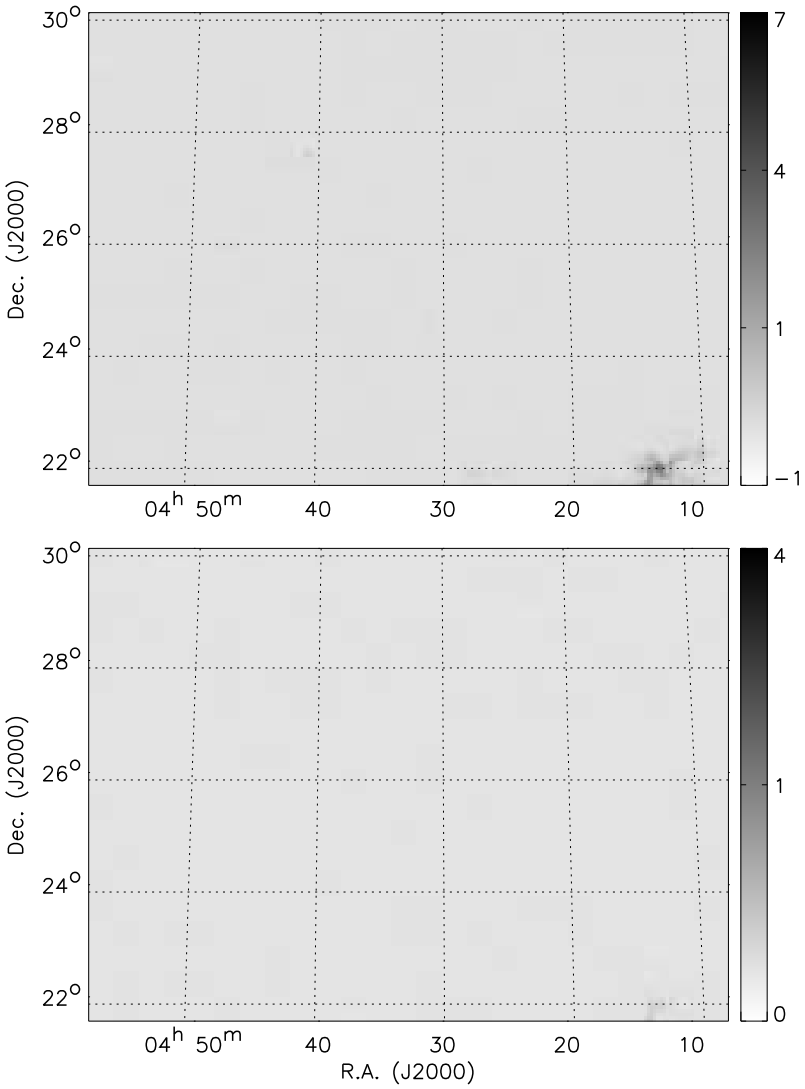

Fig. 19.— Same as Figure 7 for V_{LSR} 12 to 13 km s^{-1}.

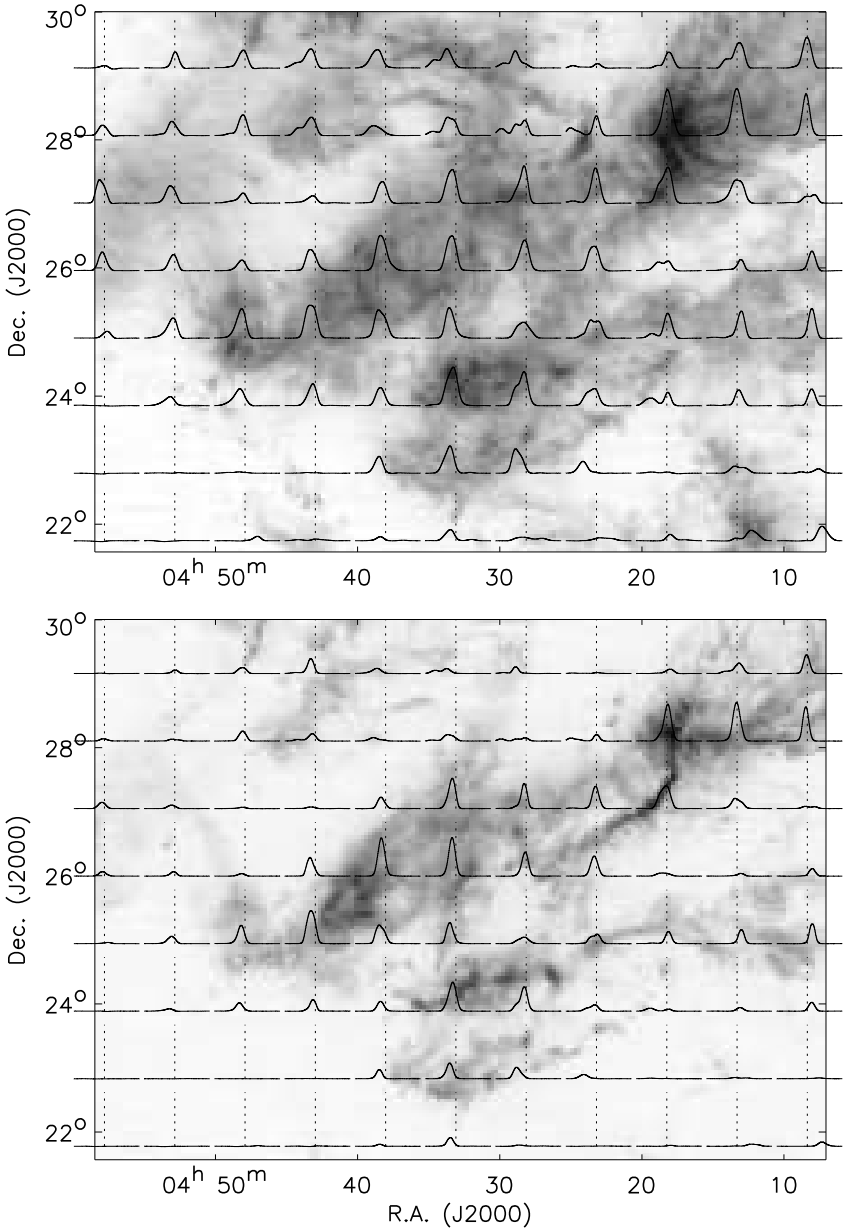

Fig. 20.— Mosaic of box-averaged spectra over the 88 hard-edged sub-cubes for ^{12}CO (top) and ^{13}CO (bottom) overlayed on images of the integrated intensity of each isotopologue. The velocity scale on the x-axis is 0 to 15 km s^{-1}, and the temperature scale ranges from -0.1 to 4.5 K for ^{12}CO and -0.005 to 2.0 K for ^{13}CO. The vertical dotted line in each spectrum denotes V_{LSR}=7.0 km s^{-1}.

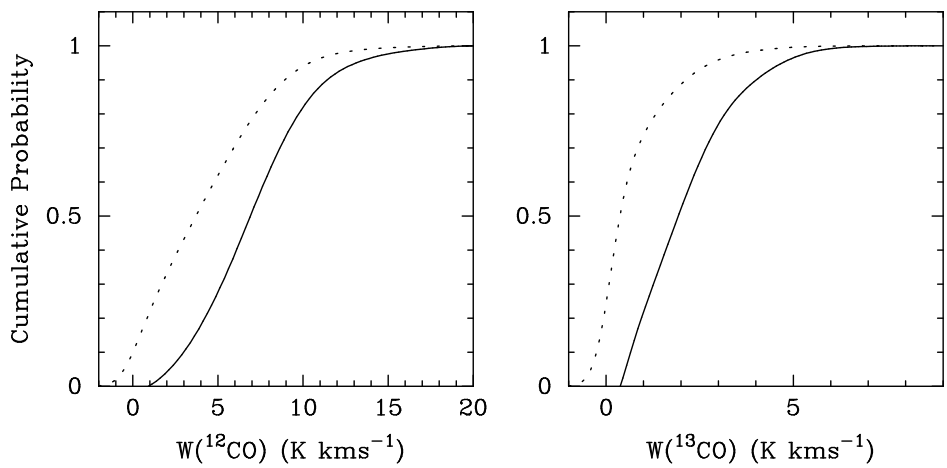

Fig. 21.— Weighted (solid line) and unweighted (dotted line) cumulative probability density functions as a function of ^{12}CO and ^{13}CO integrated intensity (denoted as W(^{12}CO) and W(^{13}CO) respectively). The unweighted and weighted cumulative PDFs describe the fractional contribution by projected area and integrated intensity emission respectively.

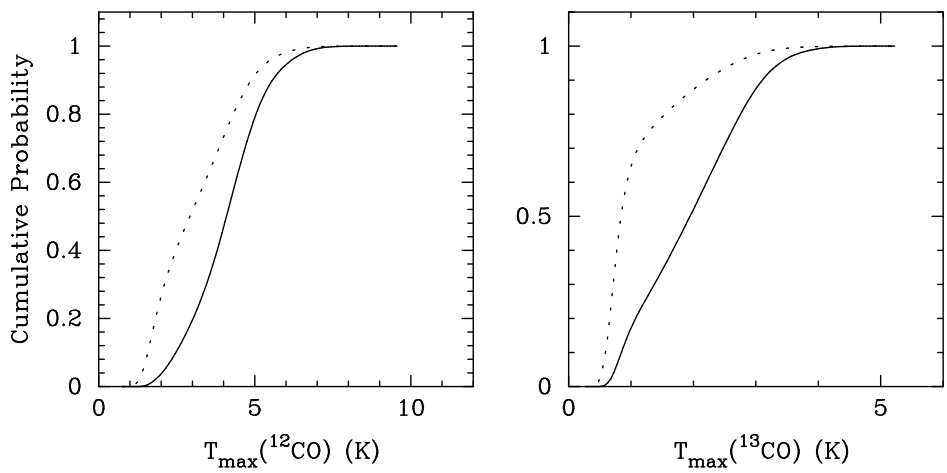

Fig. 22.— Weighted (solid line) and unweighted (dotted line) cumulative probability density functions as a function of ^{12}CO and ^{13}CO peak intensity.